Electronic Spin Alignment within Homologous $NiS_2/NiSe_2$ Heterostructures to Promote Sulfur Redox Kinetics in Lithium-Sulfur Batteries

Chen Huang, Jing Yu, Chao Yue Zhang*, Zhibiao Cui, Wei-Hong Lai, Yao-jie Lei*, Bingfei Nan, Xuan Lu, Li Gong, Junshan Li, Canhuang Li, Jin Yuan Zhou, Lluís Balcells, Jordi Arbiol, and Andreu Cabot*

C. Huang, J. Yu, B. F. Nan, X. Lu, L. Gong, C. H. Li, A. Cabot

Catalonia Institute for Energy Research-IREC

Sant Adrià de Besòs, Barcelona 08930, Spain

E-mail: acabot@irec.cat

C. Huang, L. Gong, C. H. Li

Department of Chemistry

Universitat de Barcelona 08028, Spain

J. Yu, J. Arbiol

Catalan Institute of Nanoscience and Nanotechnology (ICN2), CSIC and BIST, Campus UAB, Bellaterra, 08193 Barcelona, Catalonia, Spain.

Z. B.Cui

School of Chemistry, South China Normal University, Guangzhou 510006, PR China

C. Y. Zhang, J. Y. Zhou

Key Laboratory for Magnetism and Magnetic Materials of the Ministry of Education & School of Physical Science & Technology

Lanzhou University Lanzhou 730000, China

E-mail: zhangchy2020@lzu.edu.cn

W. H. Lai, Y. J. Lei

Institute for Superconducting and Electronic Materials

Australian Institute of Innovative Materials

Innovation Campus

University of Wollongong

Wollongong, NSW, 2500, Australia

E-mail: yl876@uowmail.edu.au

J. S. Li

Institute for Advanced Study

Chengdu University 610106, Chengdu, China

L. Balcells

Institut de Ciència de Materials de Barcelona,

Campus de la UAB, 08193 Bellaterra, Catalonia, Spain

J. Arbiol and A. Cabot

ICREA Pg. Lluis Companys, 08010 Barcelona, Catalonia, Spain

* Corresponding authors

Keywords: Lithium-sulfur battery, spin state, homologous heterostructure, nickel sulfide, nickel selenide, hollow particle, lithium polysulfide.

Abstract

The catalytic activation of the Li-S reaction is fundamental to maximizing the capacity and stability of Li-S batteries (LSBs) by blocking the migration of lithium polysulfides (LiPSs) and enhancing sulfur utilization. Current research on Li-S catalysts mainly focuses on the optimization of the energy levels to promote

adsorption and catalytic conversion of LiPSs, while frequently overlooking the electronic spin state influence on charge transfer and orbital interactions. Here, hollow $NiS_2/NiSe_2$ heterostructures encapsulated in a nitrogen-doped carbon matrix ($NiS_2/NiSe_2$@NC) are synthesized and used as a catalytic additive in sulfur cathodes. The $NiS_2/NiSe_2$ heterostructure promotes the spin splitting of the 3d orbital, driving the Ni^{3+} transformation from low to high spin, and thereby generating additional unpaired electrons. The high spin configuration orbit of $NiS_2/NiSe_2$@NC raises the electronic energy level and activates the electronic state. X-ray absorption near-edge structure (XANES), extended X-ray absorption fine structure (EXAFS) spectra, and density functional theory (DFT) results show that the activated electronic state accelerates the charge transfer and the regulated d-band center optimizes the adsorption energy, lowering the reaction energy barrier of the LiPS conversion rate-determining step (RDS). *In situ* XRD analyses further reveal that the spin polarization associated with the formed heterostructures can accelerate the sulfur conversion kinetics. Benefiting from these characteristics, LSBs based on $NiS_2/NiSe_2$@NC/S cathodes exhibit high initial capacity (1458 mAh g^{-1} at 0.1C), excellent rate capability (572 mAh g^{-1} at 5C), and stable cycling with an average capacity decay rate of only 0.025% per cycle at 1 C during 500 cycles. Even at a high sulfur loading (6.2 mg cm^{-2}), a high initial capacity of 1173 mA h g^{-1} (7.27 mAh cm^{-2}) is measured at 0.1 C, and 1058 mA h g^{-1} is retained after 300 cycles. This work not only provides an effective strategy for improving the electrochemical performance of LSBs but also shows new insights on the role of spin polarization in the field of electrocatalysis.

1. Introduction

Lithium-sulfur batteries (LSBs) hold great potential for the development of future energy storage systems for mobility and stationary applications due to their high energy density and abundant sulfur resources. However, their commercialization is currently hampered by several challenges, including:[1] 1) the migration of lithium polysulfides (LiPSs) that progressively reduce the amount of cathode active material while decreasing the electrolyte ion mobility and degrading the anode surface; 2) a poor conductivity of sulfur and lithium sulfides (Li_2S_2/Li_2S), which increase the system internal resistance and limits active material

utilization, particularly at high sulfur loadings; 3) slow Li-S redox reaction kinetics which limits the rate performance and also the amount of active material participating in each cycle; and 4) the severe volume changes during charge/discharge that reduce the LSB cycling stability.[2] Various strategies have been proposed to address these limitations, including the use of multifunctional separators[3] and particularly the incorporation of host materials and additives within the sulfur cathode.[4] High surface area and porous carbon materials are fundamental as sulfur hosts in LSB cathodes, contributing to the physical trapping of the LiPSs, the damping of the volume changes, and especially to facilitate charge transport within the electrode.[5] However, the weak chemical interaction between the nonpolar carbon surface and polar polysulfides falls short of completely inhibiting the migration of LiPS, posing a challenge in achieving stable long-term cycling.[6] Such carbon hosts are also inefficient in accelerating the Li-S redox reaction.

Polar inorganic additives can be used to promote LiPS trapping and catalyze the Li-S reaction. Among the vast array of potential catalysts, nickel-based compounds stand out due to their exceptional performance, even at low doses, which stems from nickel's notable high activity and versatility.[7] Nickel is also the fifth most abundant element on Earth, which results in a moderate cost, four orders of magnitude lower than that of platinum-group metals. Ni also offers additional oxidation states over Pt and Pd, which allows both to catalyze single electron reactions and form more diverse catalytic phases. In this direction, the redox Ni^{2+}/Ni^{3+} shows particularly high activity compared to other metal-based compounds. Besides, nickel facilitates hemolytic bond cleavage, has a strong affinity to unsaturated systems and coordination of multiple bonds, and is highly nucleophilic on account of its relatively small size, which makes it a privileged reagent for cross-coupling. On top of this, nickel shows notable electrical conductivity and resistance to bulk oxidation, which allows it to maintain good electrical conductivity under operation conditions.

Compared with oxides, chalcogenides show a lower energy gap between the bonding and antibonding orbitals, which is regulated by the chalcogen P-band.[8] At the same time, the reduced electronegativity difference between the metal and the chalcogen decreases the electron-pull effect leading to an increase in the energy of the bonding state that can enhance the interfacial S_6^{2-}/S^{2-} redox kinetics.[9]

Based on the above advantages, Ni-based chalcogenides exhibit great potential as catalytic additive to activate the Li-S reaction in LSB cathodes. In this direction, nickel sulfide displays particularly high polysulfide adsorption capability,[10] but its moderate electrical conductivity limits the electrode performance and thus

calls for an additional phase. In this regard, several heterostructured systems have been demonstrated effective in regulating the surface state of electrode materials, potentially improving both charge transport and transfer, e.g. NiS_2-WS_2,[11] NiS_2/ZnS,[12] MoS_2/NiS_2[13] and MnS/NiS_2/MoS_2.[14] However, most previous works have focused on composites comprised of different metals, a strategy that unfortunately tends to limit both the performance and stability of the resultant materials. This limitation arises from the introduction of defects, which detrimentally impact the charge transport. Furthermore, these defects and stresses can adversely affect the structural and mechanical integrity of the material, leading to a progressive performance deterioration.

Both NiS_2 and $NiSe_2$ exhibit a pyrite structure wherein Ni^{2+} ions are surrounded by six X_2^{2-} units. Despite this structural similarity, they display distinct d-electron configurations. This difference endows $NiSe_2$ with superior electrical conductivity, attributed to its more favorable electron mobility. In contrast, NiS_2 is characterized by a faster charge transfer capability.[15] These contrasting electronic properties can be synergistically integrated within homologous composites. In this direction, the versatility of nickel chalcogenides emerges as particularly advantageous. This is primarily due to the flexible valence states exhibited by nickel and the ability of chalcogenides to concatenate. As a result, it becomes feasible to engineer materials encompassing a variety of Ni/chalcogen ratios. This compositional flexibility allows for the fine-tuning of the electrochemical properties of these composites, enabling tailored optimization to meet specific performance criteria in various electrochemical applications.

While extensive research has focused on the relationship between electronic energy levels and catalytic properties, the role of electron spins in this dynamic has often been overlooked. Investigating the role of spin states of electrons, particularly in transition metal catalysts, could reveal new insights into reaction mechanisms. Furthermore, understanding spin-related phenomena could lead to the development of novel catalytic materials designed with spin considerations in mind, potentially opening new pathways in green chemistry and sustainable energy solutions. Indeed, the spin state configuration of 3d transition metals is a key factor influencing the catalyst's electronic structure and determining its orbital occupation, activity, and selectivity.[16] This spin state can be effectively adjusted through external or internal magnetic fields, the use of ligands, or stresses. [16d, 16g, 17] As an example, we recently reported that transition Co atoms experienced a spin transformation from low spin to high spin under an external magnetic field, thereby generating more

unpaired electrons to promote charge transfer within LSBs.[17b] Also within the framework of LSBs, Li et al. revealed improved catalytic activity of bimetallic phosphorus sulfides associated with their composition-determined spin state.[18]

An innovative and effective approach for manipulating the spin state of materials involves the utilization of heterointerfaces. The interface of semiconductor heterostructures is characterized by a charge redistribution that results in an internal electric field and an electronic band bending. [19] This is linked to a rise in the energy level of the 3d orbitals, thereby altering the metal-LiPS adsorption strength. In addition, the heterostructure can split the metal central orbital, thereby changing the electronic configuration from a low-spin state to a high-spin state. This transition can produce more unpaired electrons and active electronic states in the 3d orbital. This strategy offers an excellent opportunity to design catalysts with optimized catalytic performances, properly defining their spin state by combining two dissimilar materials. Despite the potential of heterointerfaces to tune spin states and particularly their role in catalytic performance, few studies have been reported in this direction, all in the paradigmatic case of the oxygen evolution reaction.[20]

Beyond composition, the structural architecture of the sulfur host material also plays a fundamental role in determining the LSB cathode electrochemical performance. A proper three-dimensional (3D) organization of the different components is essential to maximize the cathode performance, especially with the challenging high sulfur loadings. Hollow materials are particularly effective in alleviating volume changes during cycling while and the same time providing high surface areas, which makes them widely used in the fields of Li-ion batteries,[21] supercapacitors[22], and electrocatalysis.[23] The internal volume of hollow structures and their large surfaces also allow loading large amounts of sulfur.[24] Besides, hollow sulfur hosts can physically lock polysulfides, thus reducing their migration.[25]

Herein, hollow homologous heterostructure $NiS_2/NiSe_2$@NC are synthesized using a Ni-based metal-organic framework (MOF) as a sacrificial template. The electronic structure and spin state of the developed material are thoroughly characterized both experimentally and using density functional theory (DFT) calculations. Besides, $NiS_2/NiSe_2$@NC is used as the sulfur host to assemble coin- and pouch-type LSBs, whose performance is tested even under high sulfur loading (6.2 mg cm^{-2}) and lean electrolyte conditions.

2. Results and Discussions

Scheme 1 illustrates the synthesis of the $NiS_2/NiSe_2$@NC/S cathode material. The synthesis details can be found in the Experimental section within the Supporting Information (SI). Briefly, to produce $NiS_2/NiSe_2$@NC, first Ni-based hollow precursors (Ni-MOF) were prepared by a solvothermal method using trimesic acid (H_3BTC) as organic ligands, nickel(II) nitrate as the metal source and polyvinylpyrrolidone (PVP) as a stabilizer. [26] Subsequently, the Ni-MOF was heated to 500ºC under an Ar atmosphere to reduce the Ni^{2+} to metallic nickel and carbonize the organic ligands into nitrogen-doped carbon.[27] The obtained Ni/NC was then simultaneously sulfurized and selenized, using equal mass amounts of S and Se, to form the $NiS_2/NiSe_2$@NC composite. Finally, $NiS_2/NiSe_2$@NC/S was produced by introducing S through a melt-infiltration process.

Scanning electron microscopy (SEM) analysis revealed that the precursor Ni-MOF is comprised of ca. 2 μm spherical particles characterized by their smooth surfaces and a hollow internal structure (**Figure S1a**). The hollow nature of these particles was inferred from the incidental observation of a small number of particles that had fortuitously broken, thereby providing a glimpse into their internal structure. After carbonization, the obtained Ni@NC particles maintained the spherical and hollow architecture, but they significantly shrank to an average diameter of about 500 nm, due to the decomposition of the organic ligands (**Figure S1b**). After sulfuration and selenization, $NiS_2/NiSe_2$@NC retains the Ni@NC hollow morphology and size (**Figure 1b**). Energy-dispersive X-ray (EDX) spectroscopy combined with SEM imaging and electron energy loss spectroscopy (EELS) combined with high angle annular dark field (HAADF) scanning transmission electron microscopy (STEM) shows the different elements to be homogeneously distributed within the $NiS_2/NiSe_2$@NC composite at the 100 nm scale (**Figure 1c, d**). EDX spectra showed the $NiS_2/NiSe_2$@NC atomic elemental ratio to be Ni/S/Se/N = 28/50/19/3 (**Figure S2**). High-resolution TEM (HRTEM) characterization of $NiS_2/NiSe_2$@NC shows the $NiS_2/NiSe_2$@NC particles to be polycrystalline, formed by ca. 20 nm crystallites of both the NiS_2 and $NiSe_2$ phases (**Figure 1e**).

Additional $NiSe_2$@NC and NiS_2@NC reference samples were produced by just selenizing or sulfurizing the Ni/NC (see details in the SI). EDX compositional maps of these reference samples also show a homogeneous distribution of the different elements at the 100 nm scale (**Figures S3 and S4)**.

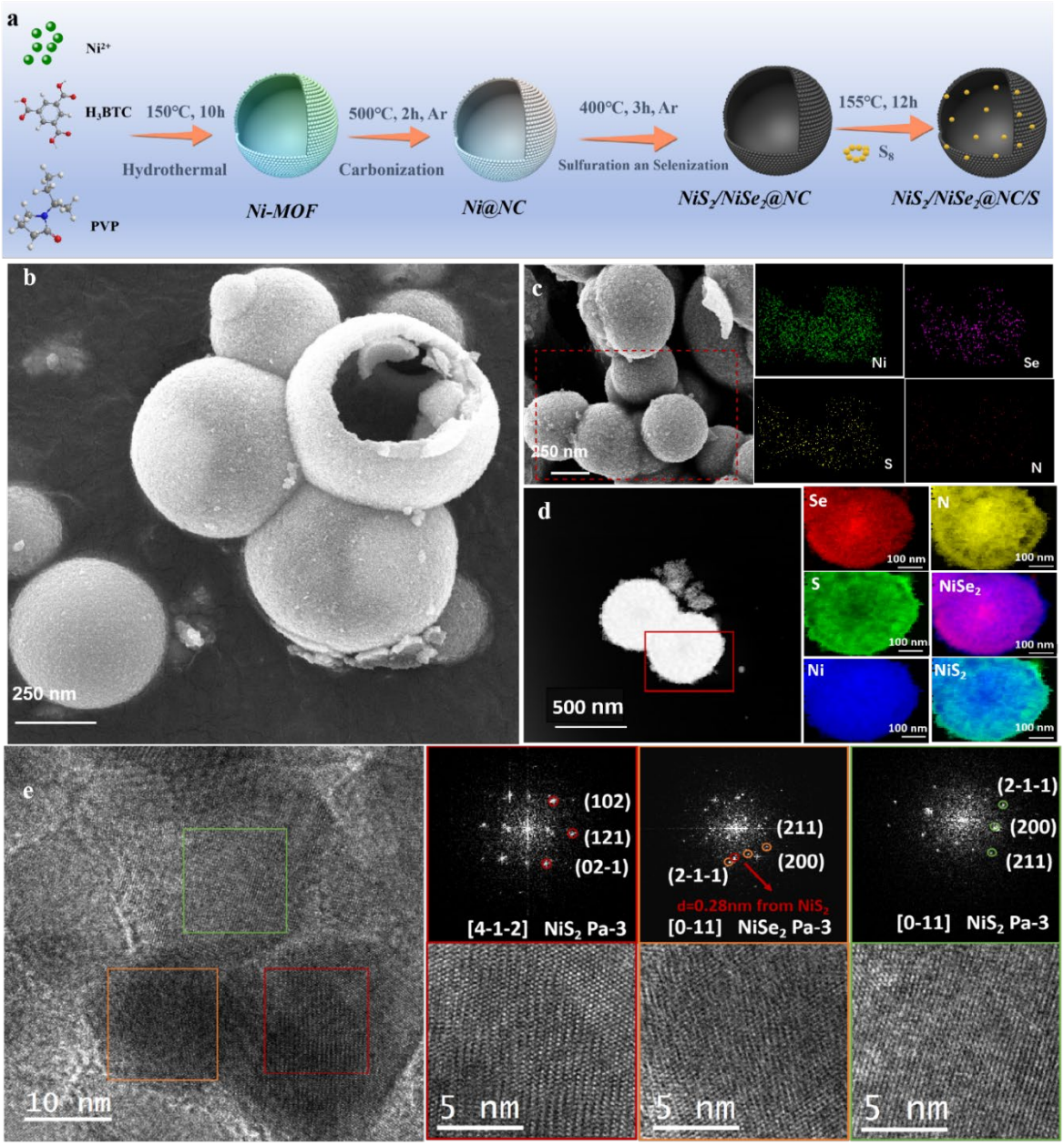

Figure 1. (a) Schematic diagram of the synthesis of the $NiS_2/NiSe_2$@NC/S cathode material. (b) SEM image of $NiS_2/NiSe_2$@NC. (c) SEM image and SEM-EDX compositional map of $NiS_2/NiSe_2$@NC. (d) HAADF STEM image and STEM-EELS composition maps of $NiS_2/NiSe_2$@NC. (e) HRTEM micrographs from the $NiS_2/NiSe_2$@NC sample and the corresponding power spectra. The lattice fringes visualized in the red squared magnified detail correspond to the (102), (121), and (02-1) crystal planes of NiS_2 visualized along the [4-1-2] zone axis. The lattice spacings shown in the orange squared detail correspond to the (211) (200), and (2-1-1) crystal planes of $NiSe_2$ visualized along its [0-11] zone axis. Besides, the lattice fringes visualized in the green squared magnified detail correspond to the (2-1-1), (200), and (211) crystal planes of NiS_2

visualized along the [0-11] zone axis.

Figure 2a shows the X-ray diffraction (XRD) patterns of $NiS_2/NiSe_2$@NC, $NiSe_2$@ NC and NiS_2@NC. The diffraction peaks at 31°, 34.7°, 38.0°, 44.3°, and 52.6°, are attributed to (200), (210), (211), (220), and (311) planes of NiS_2 (PDF #89-3058). The diffraction peaks at 30.4°, 34.1°, 37.4°, 43.5°, and 51.5° are assigned to the (200), (210), (211), (220), and (311) planes of $NiSe_2$ (PDF #88-1711). XRD data confirms the presence of both phases, as observed by HRTEM imaging, but shows the amount of NiS_2 phase to be notably higher than that of $NiSe_2$. Using the Scherrer equation (**Figure S5a)**, the size of the crystallites was estimated at ca. 20 nm, which is consistent with HRTEM results. Compared with NiS_2@NC, the peaks corresponding to the NiS_2 phase in the $NiS_2/NiSe_2$@NC XRD pattern are slightly shifted to lower angles (**Figure S5b**). At the same time, compared with $NiSe_2$@NC, the peaks corresponding to the $NiSe_2$ phase in the $NiS_2/NiSe_2$@NC XRD pattern are slightly shifted to higher angles. These shifts are consistent with the different ionic radii of Se and S and denote a substantial Se and S doping within the NiS_2 and $NiSe_2$ lattices, respectively. Using Vergard's law (**Figure S5c**), we estimated ca. 17% of S in $NiSe_2$ and ca. 21 % Se in NiS_2 within the $NiS_2/NiSe_2$@NC. On the other hand, the XRD pattern of carbon is not observed due to the good crystallinity of the Ni chalcogenides.

The degree of carbon graphitization was measured using Raman spectroscopy. The Raman peaks centered at 1350 cm^{-1} and 1590 cm^{-1} correspond to the D and G bands arising from the disordered structure and bond stretching motion of sp^2 hybridized carbon, respectively (**Figure S6**). Their intensity ratio, I_G/I_D, for $NiS_2/NiSe_2$@NC, $NiSe_2$@NC, and NiS_2@NC was 1.02, 1.03, and 1.03, respectively (**Table S1**), indicating that carbon is present in both amorphous and graphitized forms. This is convenient for electrochemical applications because while amorphous carbon can provide additional electrochemically active sites, graphitized carbon promotes charge transport.[22a]

The specific surface area was determined from N_2 adsorption/desorption isotherms using the Brunauer-Emmett-Teller (BET) calculation (**Figure S7**). The specific surface areas of $NiS_2/NiSe_2$@NC, $NiSe_2$@NC and NiS_2@NC were 166.2 $m^2\ g^{-1}$, 132.6 $m^2\ g^{-1}$ and 108.9 $m^2\ g^{-1}$ respectively. In addition, the Barrett-Joyner-Halenda (BJH) pore size distribution of the three electrode materials showed a main contribution in the micropore size range, 0-50 nm. Such large specific surface area and highly porous structure are associated with the hollow material architecture and the sulfurization/selenization processes that generate additional

pores within the structure.

X-ray photoelectron spectroscopy (XPS) shows the surface of $NiS_2/NiSe_2$@NC to be chalcogen-rich, (S+Se)/Ni = 6 (**Table S2**), with S accounting for 76 % of the surface chalcogen amount (**Figure S8**). The Ni 2p high-resolution XPS spectrum of $NiS_2/NiSe_2$@NC (**Figure 2b**) shows two doublets assigned to Ni^{2+} (Ni $2p_{3/2}$ = 853.1 eV) and Ni^{3+} (Ni $2p_{3/2}$ =855.3 eV) and two satellite peaks. Compared with NiS_2@NC and $NiSe_2$@NC, the binding energies of Ni within $NiS_2/NiSe_2$@NC are red-shifted by ca. 0.8 eV. Besides, the Ni satellite peaks of the $NiS_2/NiSe_2$@NC are significantly larger than those of $NiSe_2$@NC and NiS_2@NC (**Figures 2e and S9, and Table S3**). Generally speaking, the greater the relative Ni 2p satellite peak area, the higher its magnetic susceptibility.[4f, 28] Thus, XPS data point to $NiS_2/NiSe_2$@NC having a larger magnetic susceptibility than $NiSe_2$@NC and NiS_2@NC. The Se 3d spectrum of $NiS_2/NiSe_2$@NC shows one doublet assigned to Se^{2-} within a metal selenide chemical environment (Se $3d_{5/2}$ = 55.1 2V, **Figure 2c**). The doublet is slightly blue-shifted by 0.2 eV with respect to $NiSe_2$@NC, which is consistent with both the presence of a significant part of the total Se within the NiS_2 lattice and with some degree of charge transfer from $NiSe_2$ to NiS_2 within the $NiS_2/NiSe_2$ composite.[29] On the other hand, the S 2p spectra of the different materials show 4 doublets that can be assigned to divalent sulfide ions (S^{2-}) within the $NiSe_2$ lattice (S $2p_{3/2}$ = 160.6 eV), S^{2-} within the NiS_2 (S $2p_{3/2}$ =162.4 eV), C-S (S $2p_{3/2}$ =164.7 eV), and a SO_4^{2-} chemical ambient (S $2p_{3/2}$ =165.8 eV) generated during the surface oxidation of the NiS_2 crystallites when exposed to air during manipulation and transportation (**Figure 2d)**.[30] The S^{2-} components of $NiS_2/NiSe_2$@NC exhibited a negative shift of ca. 0.4 eV compared with NiS_2@NC, which is also consistent with the presence of large amounts of Se and the charge transfer from $NiSe_2$ to NiS_2 within the $NiS_2/NiSe_2$ composite. The C 1s XPS spectra display peaks at 284.6 eV, 286.2 eV, and 288.4 eV attributed to C=C, C-O, and C=O, respectively (**Figure S10a**). In the N 1s high-resolution XPS spectra, three peaks can be fitted at binding energies of 398.4 eV, 399.8 eV, and 402.1 eV corresponding to pyridinic-N, pyrrolic-N and graphitic-N, respectively (**Figure S10b**). As noted in previous reports, pyridinic-N can effectively increase the electron density and interact with sulfur/polysulfides, while pyrrolic-N and graphitic-N can effectively enhance the affinity of polar atoms to elemental sulfur (S_8) and polar polysulfides (Li_2S, Li_2S_2, Li_2S_4, Li_2S_6, and Li_2S_8) through strong Lewis acid-base interactions.[31]

Figure 2e and S11a shows the dependence of magnetization on the external magnetic field at 300 K of the different Ni chalcogenides. $NiS_2/NiSe_2$@NC shows a clear hysteresis loop and the largest saturation

magnetization among the tested samples, 8.32 emu g^{-1} at 100 KOe, indicating ferromagnetic behavior at ambient temperature. The zero-field cooled/field cooled (ZFC/FC) curves of $NiS_2/NiSe_2$@NC indicate a Curie temperature above 300 K (**Figure S11b**). The magnetic susceptibilities of $NiSe_2$@NC and NiS_2 @NC are much lower, at 0.81 emu g^{-1} and 0.34 emu g^{-1}, respectively, indicating a nearly paramagnetic behavior. The electron paramagnetic resonance (EPR) spectra of the Ni chalcogenides show a characteristic feature at g=2.51(**Figure 2f**), associated with unpaired electrons in the Ni 3d orbital. This feature is much more notorious in the $NiS_2/NiSe_2$@NC composite than in NiS_2@NC and $NiSe_2$@NC pointing to a higher concentration of unpaired electrons in the former.

X-ray absorption near-edge structure (XANES) and extended X-ray absorption fine structure (EXAFS) spectra were used to analyze the atomic coordination environment and chemical state of $NiS_2/NiSe_2$@NC, $NiSe_2$@NC, and NiS_2@NC (**Figure S12-14**). The XANES spectra show the Ni K-edge of $NiS_2/NiSe_2$@NC localized between that of Ni_2S_3 and the Ni foil, indicating an intermediate chemical state of Ni. The absorption edge of the Ni K-edge in $NiS_2/NiSe_2$@NC is slightly red-shifted relative to $NiSe_2$@NC and NiS_2@NC, which is consistent with XPS results. The Fourier transform extended X-ray absorption fine structure (FT-EXAFS) of $NiS_2/NiSe_2$@NC shows characteristic peaks at 2.43 Å and 2.52 Å corresponding to the Ni-S and Ni-Se bonds. The EXAFS fitting curve reveals that the coordination number of Ni is around 2 for Ni-S and Ni-Se in $NiS_2/NiSe_2$@NC (**Figure 2g-j**). In addition, the wavelet transform (WT) contours of Ni show a maximum intensity of around 4 $Å^{-1}$ (**Figure 2k-m**), corresponding to Ni-S and Ni-Se in $NiS_2/NiSe_2$@NC.

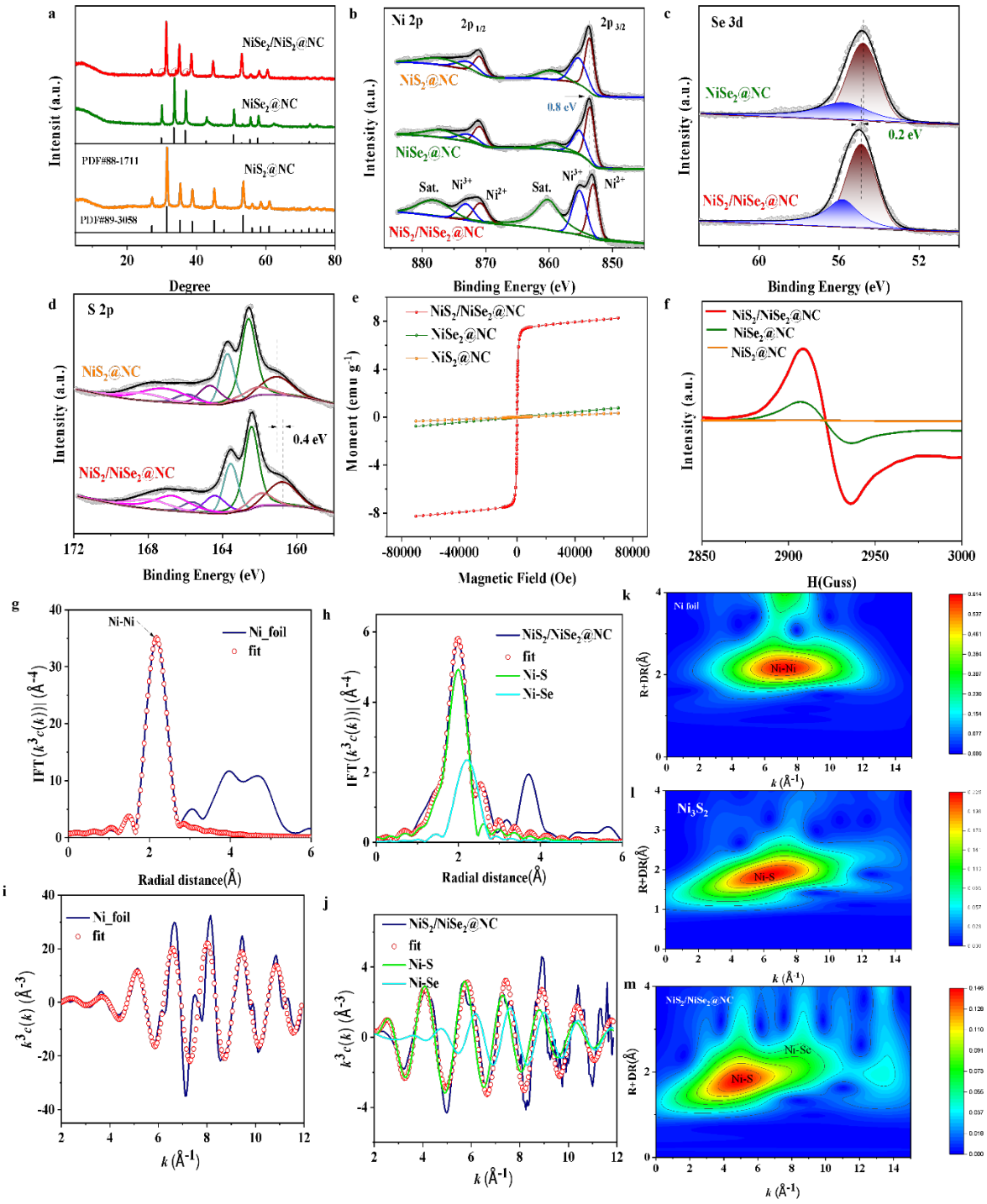

Figure 2. Structural and chemical characterization of $NiSe_2/NiS_2$@NC, $NiSe_2$@ NC, and NiS_2@NC. (a) XRD patterns. (b-d) High-resolution Ni 2p (b), Se 3d (c), and S 2p (d) XPS spectra. (e) Dependences of magnetization on the external magnetic field for $NiS_2/NiSe_2$@NC, $NiSe_2$@NC, and NiS_2@NC at room temperature (300 K). (f) EPR spectra for $NiS_2/NiSe_2$@NC, $NiSe_2$@ NC and NiS_2@NC. (g) FT-EXAFS fitting curves of Ni K-edge for Ni foil. (h) FT-EXAFS fitting curves of Ni K-edge for $NiS_2/NiSe_2$@NC.

(i) XAFS fitting curves of Ni K-edge for Ni foil (K_3 space). (j) XAFS fitting curves of Ni K-edge for $NiS_2/NiSe_2$@NC (K_3 space). (k-m) WT contour plots for Ni foil, Ni_2S_3, and $NiS_2/NiSe_2$@NC at R space.

DFT calculations were used to evaluate the interaction between LiPSs and Ni within each of the materials. First, we calculated the most stable structure of the interphase between NiS_2 (210) and $NiSe_2$ (210). Within this most stable interface, we analyzed the spin state directions before polysulfide adsorption (**Figure 3a**). The computational results reveal the presence of two distinct electron spin state regions (spin up and spin down) within the $NiS_2/NiSe_2$ host material at the very interface of the two chalcogenides. Upon introducing the adsorbing polysulfide (Li_2S_4), a pronounced charge exchange phenomenon is calculated (**Figure 3b**). Notably, a portion of the electrons at the catalyst surface transfers to the polysulfide. In parallel, the electronic spin within the heterojunction loses its order. Furthermore, an examination of the Ni spin electron density (black dotted frame) reveals $NiS_2/NiSe_2$ to present a much stronger intensity compared with NiS_2, $NiSe_2$, and polysulfides. Thus, we conclude that the spin-charge interaction within the heterostructure is notably higher compared with the pure materials. The strong interaction of Ni ions with polysulfides and the change of electron spin points at Ni as the reaction active sites. Thus, additional DFT calculations to measure the impact of heterostructure on catalytic reactions are focused on them.

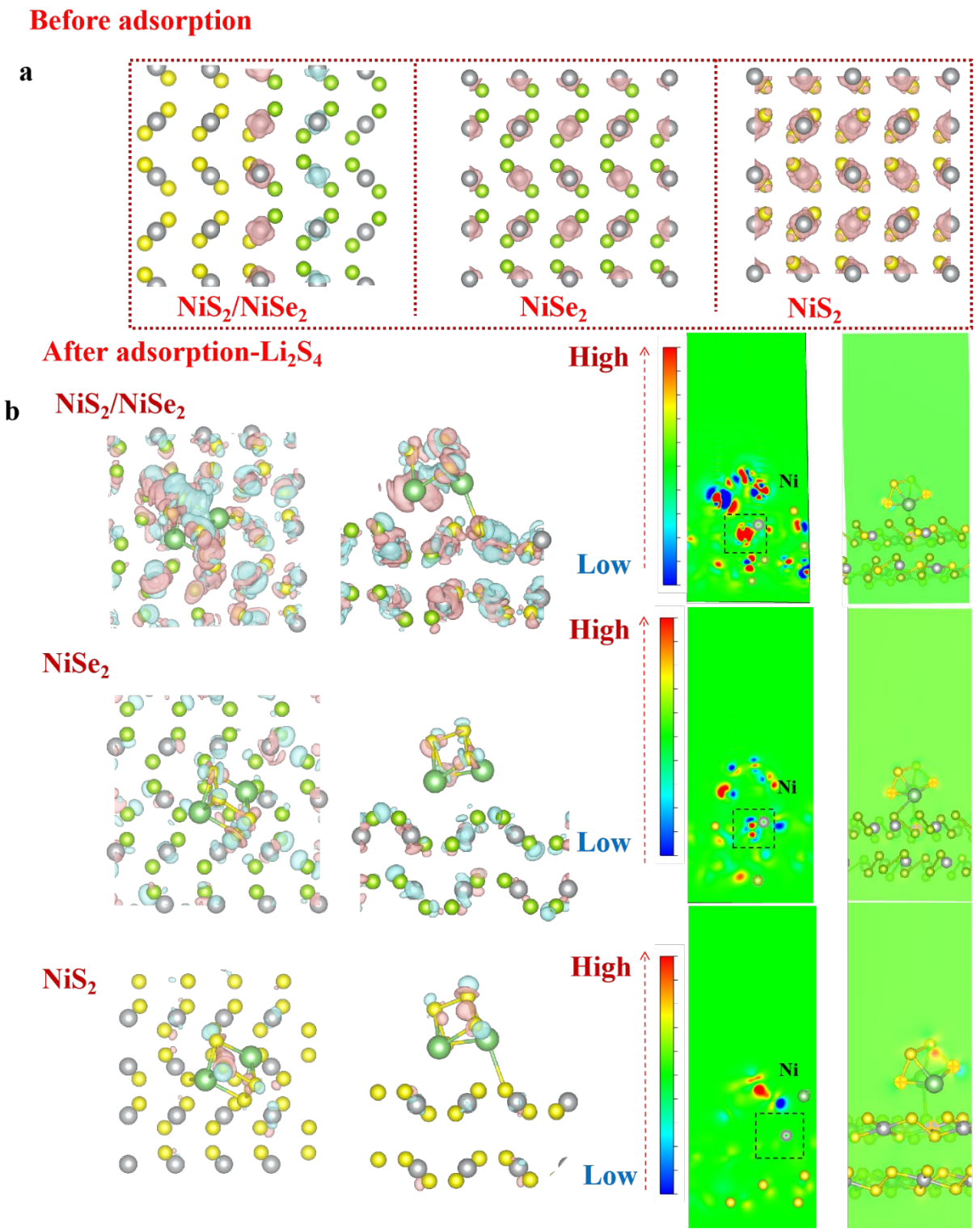

Figure 3 (a,b) Spin density of $NiS_2/NiSe_2$, $NiSe_2$, and NiS_2 before (a) and after (b) the adsorption of Li_2S_4. Grey = Ni; green = Se; yellow = S; blue = down spin state; and red = up spin state.

DFT calculations were further used to gain insight into the heterostructure electronic properties and their effects. According to DFT calculations results, the total density of states (TDOS) of $NiSe_2/NiS_2$ was more concentrated at the Fermi level compared to NiS_2 and $NiSe_2$ (**Figure 4a-b**), indicating promoted charge transport and transfer. While NC plays a dominant role in the charge transport properties of the composites,[32] four-point conductivity tests on the printed electrodes showed notable differences between the chalcogenide composites. $NiSe_2/NiS_2$@NC showed a significantly higher electrical conductivity (**Figure 4c**), at 5.4×10^2 S cm^{-1}, than $NiSe_2$@NC, at 3.6×10^2 S cm^{-1}, and particularly NiS_2@NC, at 1.4×10^2 S cm^{-1}. These results are consistent with the DFT results. This increase in the TDOS near the Fermi level was also confirmed using UV-vis spectroscopy. Tauc plots from UV−vis absorption spectra are shown in **Figure 4d-f**. The experimental band gap of the heterostructured material, $NiS_2/NiSe_2$@NC (E_g= 1.75 eV), was lower than that of each of the components, $NiSe_2$@NC (E_g= 2.01 eV) and NiS_2 (E_g = 2.06 eV).

The electron gain and loss near the interface were also determined by DFT calculations using theoretical $NiSe_2$ and NiS_2 slab models. As shown in **Figure 4g**, the differential distribution of charges indicates that electrons are transferred across the heterointerface of $NiSe_2$ and NiS_2. The charge redistribution on the $NiS_2/NiSe_2$ interface and the electron transfer between different atoms were quantitatively determined by Bader charge analysis (**Figure 4h**). Bader charge analysis showed the acquisition of 0.59 electrons by the NiS_2 unit from the $NiSe_2$ layer for $NiS_2/NiSe_2$. The gain of electrons by NiS_2 coming from $NiSe_2$ is consistent with XPS results. Overall, DFT calculations showed the formation of the heterostructure results in a notable charge redistribution between the phases.

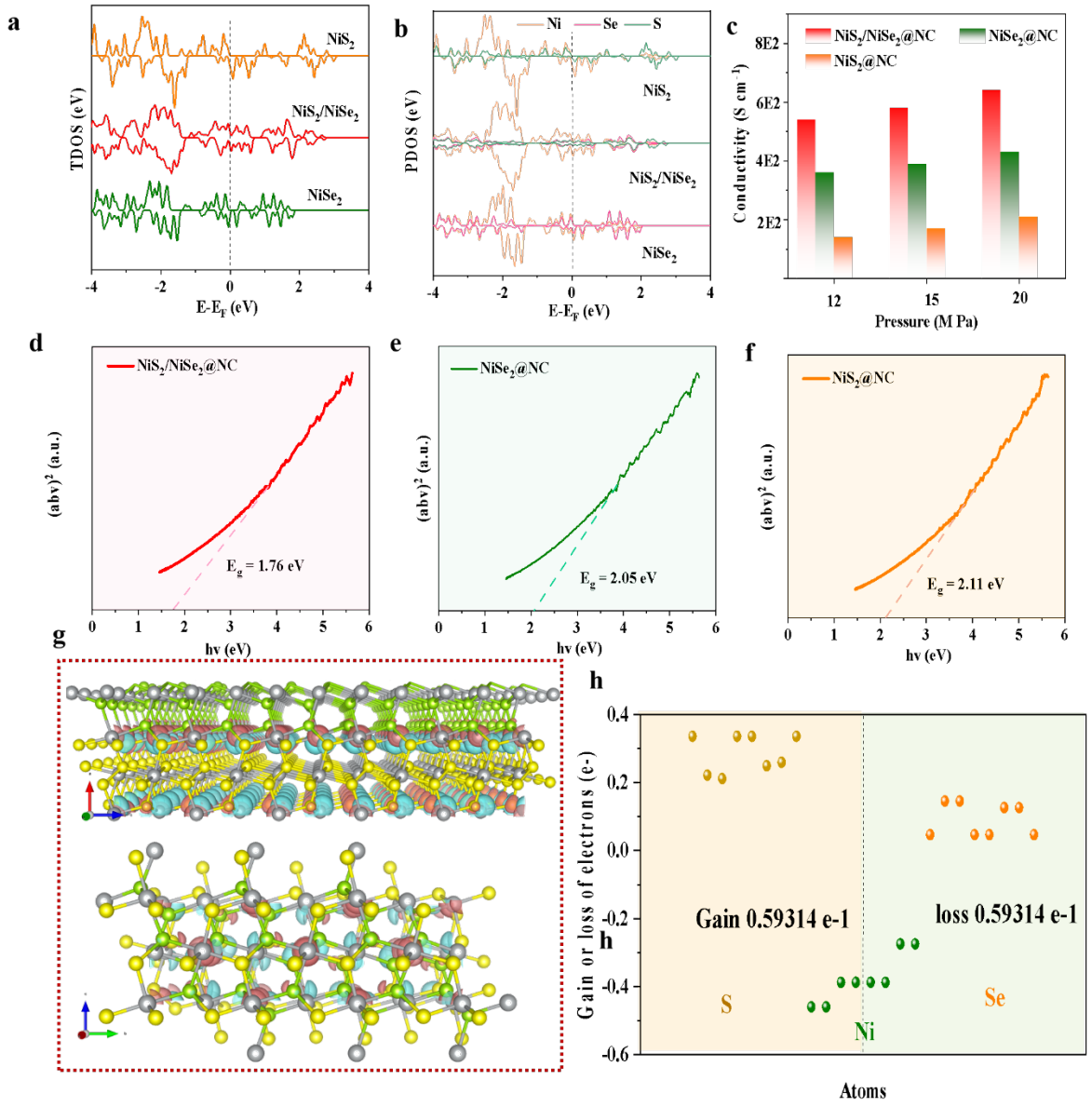

Figure 4. (a) Total density of states (TDOS) and (b) partial density of states (PDOS) of $NiSe_2/NiS_2$, $NiSe_2$, and NiS_2. (c) Electrical conductivity of $NiS_2/NiSe_2$, $NiSe_2$, and NiS_2 tested using four probes at different pressures. (d-f) Tauc plots of $NiS_2/NiSe_2$@NC (d), $NiSe_2$@NC (e), and NiS_2@NC (e). (g,h) Electron gain/loss of different atoms calculated by Bader charge analysis. Blue and red colors represent the gain and loss of electrons, respectively. Green = Se; Grey = Ni; Yellow = S.

To evaluate the potential of sulfur host materials to confine LiPSs, their Li_2S_6 adsorption capacity was tested. Optical images of vials containing a 10 mM solution of Li_2S_6 and 15 mg of $NiS_2/NiSe_2$@NC, $NiSe_2$@NC, or NiS_2@NC after overnight adsorption are shown in **Figure 5a**. Significant color differences were observed

between the different vials. In the absence of an adsorber, the Li_2S_6 solution exhibits an intense orange color. After overnight adsorption, the solution containing $NiS_2/NiSe_2$@NC shows a pale yellow color indicating that most of the Li_2S_6 has been adsorbed. In contrast, the solutions containing $NiSe_2$@NC and NiS_2@NC maintain a strong orange aspect, indicating a moderate Li_2S_6 trapping effectiveness. The UV-vis spectra of the supernatants confirmed these results and allowed quantifying the Li_2S_6 absorbance by following the light absorption in the 350-400 nm region. The chemical interaction between Li_2S_6 and $NiS_2/NiSe_2$@NC was further evaluated by XPS analysis (**Figure 5b**). In the high-resolution Ni 2p XPS spectrum of the material after Li_2S_6 adsorption ($NiS_2/NiSe_2$@NC-Li_2S_6), the two doublets at 852.9 eV and 854.6 eV ($2p_{3/2}$) are assigned to Ni^{2+} and Ni^{3+}. The two chemical states appear red-shifted when compared to the fresh $NiS_2/NiSe_2$@NC. This redshift is attributed to the S/Se-Li bond formation, which reduces the electronegativity of the Ni chemical environment.[32] In addition, compared with $NiS_2/NiSe_2$@NC, the ratio of the satellite peak area of $NiS_2/NiSe_2$@NC-Li_2S_6 is significantly reduced, which is attributed to the transfer of electrons from the heterointerface to the empty polysulfides orbitals, resulting in a reducent amount of unpaired electrons.

DFT calculations were further used to gain an understanding of the LiPS adsorption capacity of the host materials. The adsorption models of NiS_2, $NiSe_2$, and $NiS_2/NiSe_2$ with the different sulfur species (Li_2S, Li_2S_2, Li_2S_4, Li_2S_6, Li_2S_8, and S_8) are shown in **Figures S15-20 and 5c**. DFT results show that the LiPSs binding energy to $NiS_2/NiSe_2$ is higher than that of $NiSe_2$ and NiS_2. In particular, the adsorption energy between $NiS_2/NiSe_2$ and Li_2S_6 is -0.22 eV, significantly above (in absolute value) that of $NiSe_2$, at -0.18eV, and NiS_2, at -0.034 eV.

To study the electrochemical performance of the different chalcogenide composites, they were infiltrated with S to obtain $NiS_2/NiSe_2$@NC/S, $NiSe_2$@NC/S and NiS_2@NC/S. When sulfur is loaded, $NiS_2/NiSe_2$@NC/S effectively inherits the morphology of $NiS_2/NiSe_2$@NC (**Figure S21**). Upon the introduction of sulfur, the specific surface area of $NiS_2/NiSe_2$@NC/S is significantly reduced (10.3 $m^2 g^{-1}$) when compared with that of $NiS_2/NiSe_2$@NC (166.2 $m^2 g^{-1}$), indicating that sulfur is effectively confined in the pores of the host material by the simple melting infiltration strategy used (**Figure S22**). In addition, XRD characterization further shows that the crystalline S phase exists within $NiS_2/NiSe_2$@NC/S, $NiSe_2$@NC/S, and NiS_2@NC/S. Besides, thermogravimetric analysis (TGA) quantified the content of S in $NiS_2/NiSe_2$@NC/S, $NiSe_2$@NC/S, and NiS_2@NC/S is 73.8%, 71.3%, and 70.1% respectively (**Figure S23**).

To investigate the reaction mechanism within the different chalcogenides and particularly the LiPS evolution during charge and discharge processes, *in situ* synchrotron XRD (λ=0.6883 Å) patterns were collected (**Figure 5d)**. From the $NiS_2/NiSe_2$@NC/S electrode, an XRD peak at ~24.6º on the fresh cell was indexed to S_8. During discharging, S_8 disappears while a new peak appears at ~28.1º, coinciding with the formation of long-chain polysulfides. With further discharge, long-chain polysulfides gradually convert into short-chain S species and finally Li_2S, with peaks located at 30.6º and 24.9º, respectively. Upon charging to 2.8 V, Li_2S undergoes a reversible process, gradually being reduced to short-chain polysulfides, long-chain polysulfides, and finally S_8, demonstrating the fast sulfur reaction kinetics in $NiS_2/NiSe_2$@NC/S cells. In contrast, for the $NiSe_2$@NC/S and NiS_2@NC/S electrodes, a small amount of S_8 was detected throughout the entire discharge process, indicating that the catalytic ability of these two electrodes cannot completely convert S_8 (**Figures 5e and 5f)**. Besides, after charging, in both electrodes the presence of Li_2S was still detected, indicating that the catalytic ability of the catalyst is not sufficient to fully convert solid Li_2S into S. After long-term cycling, this will cause solid sulfides to slowly accumulate on the surface of the positive electrode, leading to performance decay.

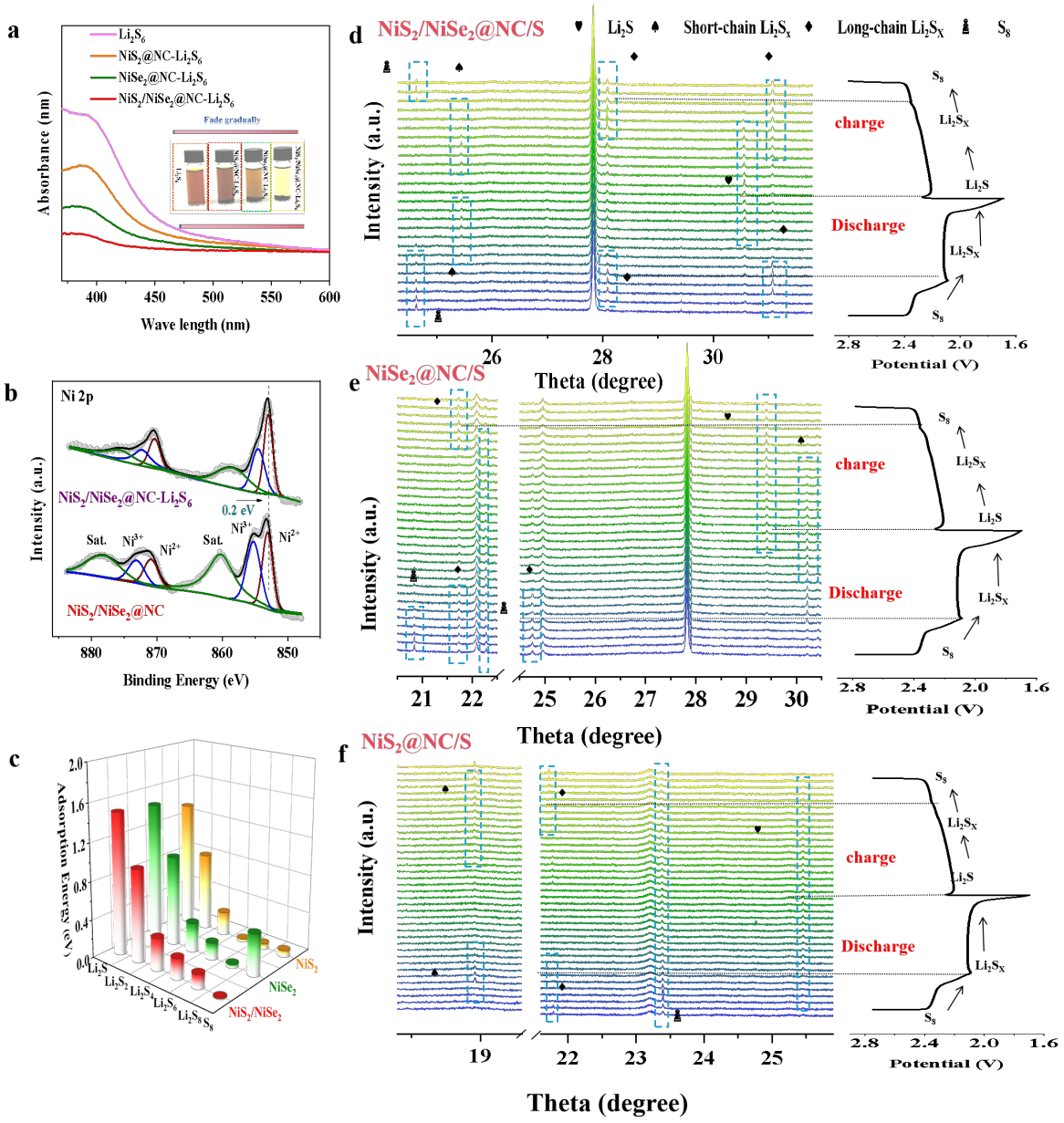

Figure 5. (a) UV-vis absorption spectra and photographs (inset) of the Li_2S_6 solutions containing different adsorbing materials after overnight adsorption. (b) High-resolution XPS spectra of Ni 2p before and after Li_2S_6 adsorption. (c) Adsorption energies of electrode materials with different polysulfides (S_8, Li_2S_8, Li_2S_6, Li_2S_4, Li_2S_2 and Li_2S). (d-f) *In situ* XRD patterns during charging and discharging of batteries based on $NiS_2/NiSe_2$@NC/S (d), $NiSe_2$@NC/S (e), and NiS_2@NC/S (f) cathodes

To evaluate the electrocatalytic activity of the chalcogenides, symmetric cells were assembled using a 0.5 M Li_2S_6 electrolyte, and the different composite materials in both electrodes. As shown in **Figure 6a**, the

cyclic voltammetry (CV) curves of the symmetric cell based on $NiS_2/NiSe_2$@NC electrodes showed the highest peak current densities, suggesting a higher activity towards the polysulfide conversion. When similar experiments were performed on $NiS_2/NiSe_2$@NC electrodes without Li_2S_6, the CV curves exhibited a rectangular shape, which was attributed to a purely capacitive behavior, indicating that Li_2S_6 was the electrochemically active species in the system.

Generally, the performance of LSBs strongly depends on their Li_2S nucleation/deposition process. The Li_2S deposition process was evaluated by first discharging the cell at a constant current (0.112 mA) to 2.06 V and then depositing Li_2S at 2.05 V. According to Faraday's law, the capacity (Q) of Li_2S deposition was calculated as $Q = It$, where I and t are the discharge current and time, respectively (**Figure 6b**). Compared to $NiSe_2$@NC and NiS_2@NC, $NiS_2/NiSe_2$@NC displayed the fastest Li_2S deposition. More importantly, the deposition capacity of Li_2S on $NiS_2/NiSe_2$@NC was the highest, at 238.8 mAh g^{-1}, compared to $NiSe_2$@NC (204.2 mAh g^{-1}) and NiS_2@NC (184.8 mAh g^{-1}). Tafel plot analysis (**Figure 6c-d**) further revealed that the $NiS_2/NiSe_2$@NC electrode is characterized by the fastest reaction kinetics with a Tafel slope of 27.4 mV dec^{-1}, well below that of $NiSe_2$@NC (53.5 mV dec^{-1}) and NiS_2/@NC (70.9 mV dec^{-1}).

DFT calculations were further used to study the S-S bond breaking at the surface of the different host materials (**Figures 6e, f and S24**). At the catalyst surface, bonds within adsorbed species are modified, displaying significant changes in the electronic density of the bonding (σ) and anti-bonding (σ*) states around the Fermi level. Compared with NiS_2@NC and $NiSe_2$@NC, the PDOS of $NiS_2/NiSe_2$@NC is shifted upward, thereby reducing the stability of the S-S bond. Thus $NiS_2/NiSe_2$@NC facilitates the breakage of S-S bonds and thus promotes the Li-S reaction kinetics.

The Gibbs free energy evolution during the reduction process on the surface of $NiS_2/NiSe_2$@NC, $NiSe_2$@ NC, and NiS_2@NC was further evaluated using DFT calculations. The models and free energy distribution of polysulfide intermediates are shown in the **Figure 6g**. The lithiation pathway from S_8 to Li_2S includes several steps. First, two Li^+ react with S_8 to generate Li_2S_8. In subsequent steps, Li_2S_8 evolves to Li_2S_6, Li_2S_4, Li_2S_2, and finally Li_2S. According to previous reports, the solid-state reaction involved in the reduction of Li_2S_2 to Li_2S plays a key role in defining the lithiation kinetics and its stability.[33] For this step, the Gibbs free energy change calculated on the surface of the $NiS_2/NiSe_2$@NC (0.68 eV) sample is sensibly lower than that of $NiSe_2$@NC (0.70 eV) and NiS_2@NC (0.70 eV).

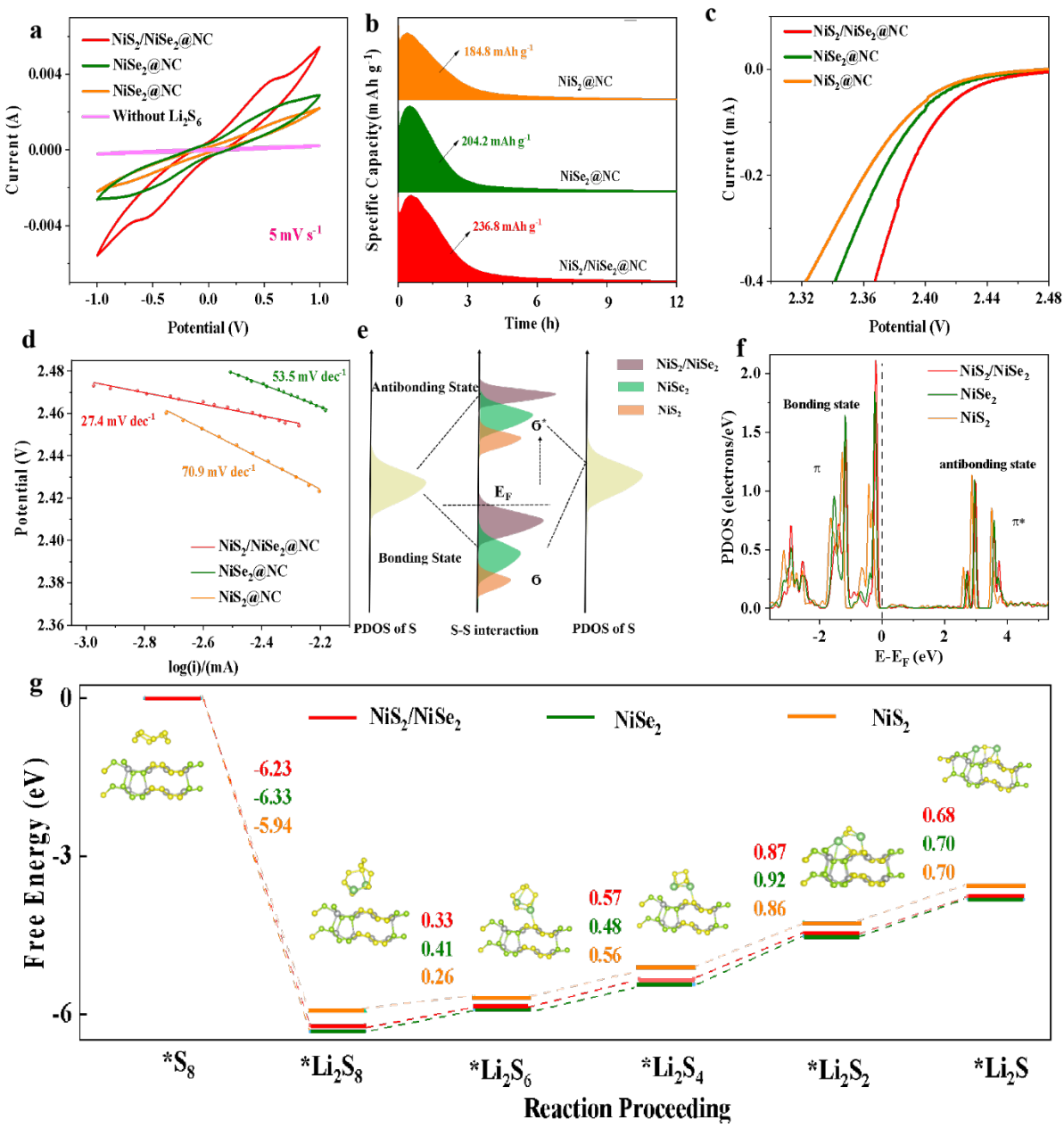

Figure 6. (a) CV curves of symmetrical cells assembled using two $NiS_2/NiSe_2$@NC, $NiSe_2$@ NC or NiS_2@NC-based electrodes. (b) Potentiostatic discharge curves on different electrodes for studying the nucleation kinetics of Li_2S. (c) LSV polarization curves $NiS_2/NiSe_2$@NC, $NiSe_2$@ NC and NiS_2@NC. (d) Tafel plots of $NiS_2/NiSe_2$@NC, $NiSe_2$@ NC and NiS_2@NC. (e-f·) Energy level diagram showing orbital hybridization for S-S. E_F is the Fermi level of the substrate; σ and σ* represent bonding and antibonding states, respectively. (g) Gibbs free energy profiles and optimized adsorption model of LiPS species on $NiS_2/NiSe_2$, $NiSe_2$, and NiS_2.

To study their electrochemical performance, coin-type cells were assembled using a nickel

chalcogenide-based sulfur cathode ($NiS_2/NiSe_2$@NC/S, $NiSe_2$@NC/S and NiS_2@NC/S), lithium foil as anode, and a solution of 1.0 M lithium bis(trifluoromethanesulfonyl) imide and 0.2 M $LiNO_3$ in a mixture of 1,3- dioxfolane (DOL) and1,2-dimethoxyethane (DME) with a volume ratio of 1:1 as electrolyte (see details in the SI). The galvanostatic charge-discharge (GCD) curves of the prepared electrode at 0.1C are shown in **Figure 7a**. All the discharge curves exhibit two distinct voltage plateaus, corresponding to the transitions $S_8 \rightarrow Li_2S_6 \rightarrow Li_2S_4$ and $Li_2S_4 \rightarrow Li_2S_2 \rightarrow Li_2S$. We define the capacity of the first plateau as Q1 and that of the second plateau as Q2. In contrast, only one charging platform is attributed to the polysulfide oxidation to S_8.[32] Compared with other sulfur cathodes, $NiS_2/NiSe_2$@NC/S exhibits the highest initial specific capacitance (1458 mAh g^{-1}), well above that of $NiSe_2$@NC/S (1326 mAh g^{-1}), NiS_2@NC/S (1150 mAh g^{-1}, **Table S4**) and most previously reported cathodes (**Figure S25 and Table S5**).[34] As the current density increases, from 0.1C to 0.2C, 0.5C, 1C, 2C, 3C, and 5C, the specific capacitance of the $NiS_2/NiSe_2$@NC/S cathode decreases from 1458 mAh g^{-1} to 539 mAh g^{-1} (**Figure 7b**). Even at 5C, the GCD curve of $NiS_2/NiSe_2$@NC/S maintains two clear discharge plateaus. When the current rate returns to 0.2C, a high specific capacity of 1050 mAh g^{-1} can still be obtained. As shown in **Figures 7c, d and S26**, the rate performance of the $NiS_2/NiSe_2$@NC/S cathode is improved over those of NiS_2@NC/S and $NiSe_2$@NC/S electrodes. Besides, $NiS_2/NiSe_2$@NC/S exhibits a smaller polarization voltage, at 131 mV, compared to $NiSe_2$@NC/S (173 mV) and NiS_2@NC/S (183 mV) (**Figure 7e**). The polarization voltage (ΔE) is here defined as the potential difference between the charge and discharge platforms at 50% charge/discharge capacity.[35] The ratio of the capacities of each discharge plateau, Q2/Q1, provides another measure of the catalytic activity of the cathode material toward the LiPSs conversion. Q_1 accounts for the sulfur reaction with Li^+ ions to soluble high-order LiPSs.[1a] Q_2 accounts for the conversion of the soluble LiPS to solid Li_2S/Li_2S_2. The theoretical Q_2/Q_1 ratio is 3, but due to the migration of a fraction of the soluble polysulfides and the incomplete Li_2S_2 to Li_2S solid-state reaction, experimental Q_2/Q_1 ratios are always below 3. Thus, Q_2/Q_1 provides a measure of the effectiveness of the conversion of S to Li_2S. Consistent with previous results, $NiS_2/NiSe_2$@NC/S exhibits a higher Q_2/Q_1 value (2.68) than $NiSe_2$@NC/S (2.47) and NiS_2@NC/S (2.13). Overall, these results confirm the effective role played by $NiS_2/NiSe_2$@NC in promoting the Li-S reaction kinetics for LSBs.

Consistently with the GCD cures, CV curves at 0.1 mV s^{-1} display two cathodic peaks, C_1 and C_2, that account

for the reduction of S_8 to highly soluble LiPSs and precipitated Li_2S_2/Li_2S, respectively **(Figure 7f**). On the other hand, only one broad anodic peak, A, is associated with the oxidation of polysulfides to S_8.[36] Compared with $NiSe_2$@NC/S and NiS_2@NC/S, NiS_2/$NiSe_2$@NC/S exhibits the highest peak currents, and the lowest oxidation peak and highest reduction peak potentials. Besides, the NiS_2/$NiSe_2$@NC/S cathode shows the highest cathodic and the lowest anodic peak onset potentials at a current density 10 μA cm^{-2} above the baseline current (**Figure S27 and 7g**).[37]

The CV curves at a scan rate of 0.1-0.4 $mV\ s^{-1}$ within a voltage window 1.7-2.8 V are shown in **Figure S28**, As the scan rate increases, the current response gradually increases. All the cathodes tested displayed a linear relationship between the peak current (I_p) and the square root of the scan rate (v), implying a diffusion-limited response (**Figure 7h**). Thus, the Li^+ diffusion coefficient (D_{Li+}) was calculated by the Randles Sevcik equation[38]:

$$I_p=2.69\text{x}10^5\ n^{1.5} A\ D_{Li}{}^{+0.5} C_{Li}{}^{+}\ v^{0.5}$$

where n, A, and C_{Li+} are the number of charges involved in the reaction, the electrode area, and the concentration of Li^+, respectively. For the NiS_2/$NiSe_2$@NC/S electrode, the D_{Li+} estimated from the two cathodic peaks and the anodic peak are $1.89\times10^{-7} cm^2\ s^{-1}$, $3.52\times10^{-7}\ cm^2\ s^{-1}$, and 5.54×10^{-7} $cm^2\ s^{-1}$, respectively. These values are significantly larger than those obtained for the other chalcogenide-based cathodes tested (**Figure S29**).

As shown in **Figure 7i**, the Nyquist plot of the electrochemical impedance spectroscopy (EIS) spectra of the different cathodes exhibits a semicircle in the high-frequency region and a straight line in the low-frequency region. The semicircle in the high-frequency region accounts for the charge transfer resistance, and the straight line in the low-frequency region is related to the diffusion resistance.[32] Among the electrodes tested, NiS_2/$NiSe_2$@NC/S was characterized by the smallest semicircle and highest slope in the high and low regions, respectively, indicating the smallest charge transfer and diffusion resistances.

To evaluate the cycling stability of different sulfur cathode materials, 500 continuous GCD cycles were tested at a current density of 1C (**Figure 7j**). NiS_2/$NiSe_2$@NC/S exhibits a higher initial capacity compared to $NiSe_2$@NC/S and NiS_2@NC. Besides, NiS_2/$NiSe_2$@NC/S also exhibits a higher capacity retention, at 87.0%, compared with $NiSe_2$@NC/S (60.6%) and NiS_2@NC/S (23.1%) after 500 cycles (**Figure S30**). After 1000 cycles

at 3C, the $NiS_2/NiSe_2$@NC cell displays a capacity decay rate of just 0.058% per cycle (**Figure 7k**).

After 100 cycles, the coin cell was disassembled and analyzed. Compared with $NiSe_2$@NC/S and NiS_2@NC/S, the separator of the post-mortem $NiS_2/NiSe_2$@NC/S cell was almost transparent, indicating that a minimal amount of LiPS had reached the membrane (**Figure S31**). Moreover, the Li anode of the cycled $NiS_2/NiSe_2$@NC/S coin cell exhibited lower corrosion and S concentration, as shown in **Figures S32 and S33**.

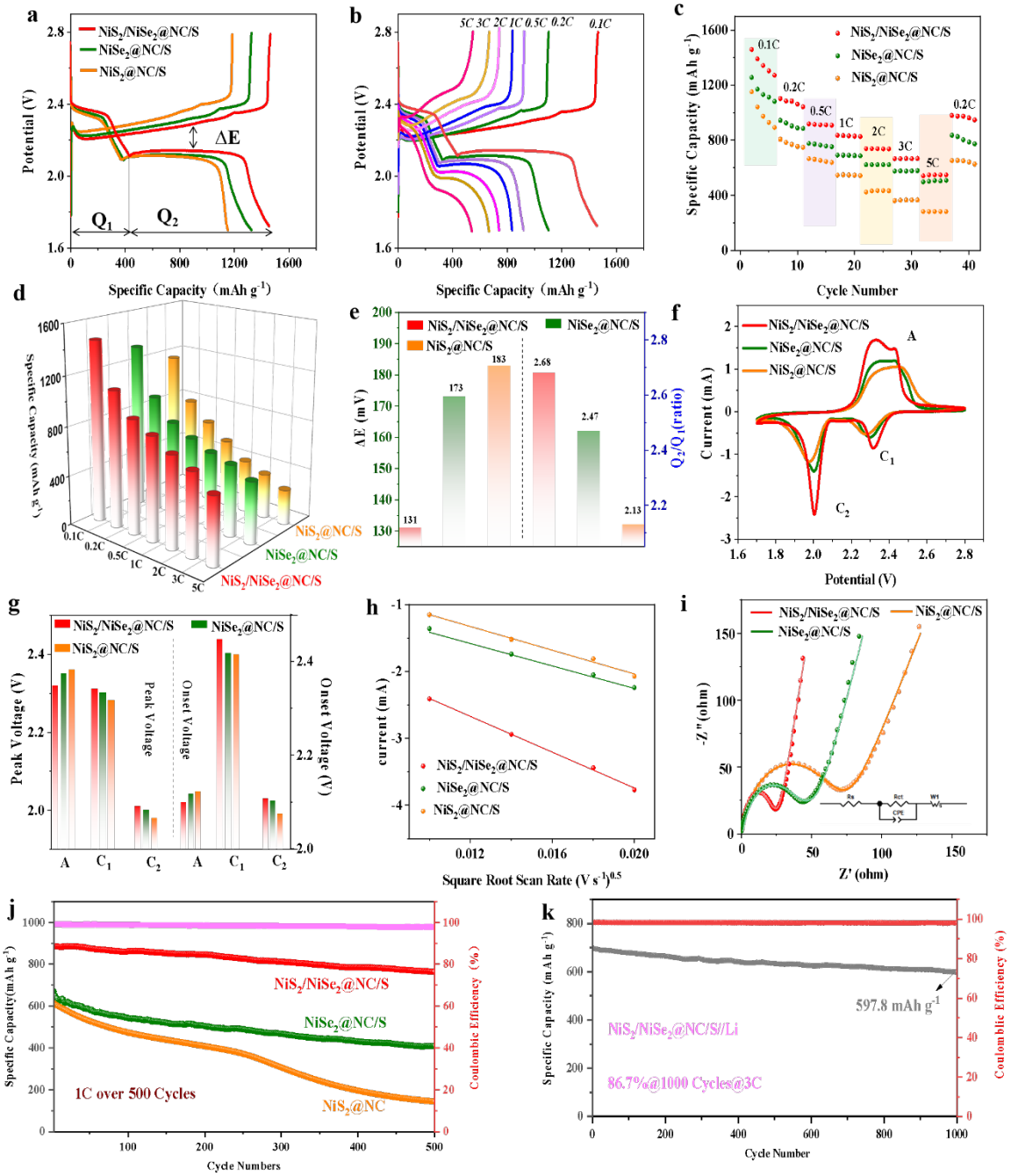

Figure 7. Coin cell characterization. (a) GCD curves of $NiS_2/NiSe_2$@NC/S, $NiSe_2$@NC/S, and NiS_2@NC/S cells

at a current rate of 0.1C. (b) GCD curve of the $NiS_2/NiSe_2$@NC/S cell at current rates in the range from 0.1C to 5C. (c) ΔE and Q_2/Q_1 values. (d-e) Rate performance. (f) CV curves of $NiS_2/NiSe_2$@NC/S, $NiSe_2$@NC/S, and NiS_2@NC/S at 0.1 mV s^{-1}. (g) Peak and onset potentials. (h) Peak current vs. square root curve of scan rate. (i) Nyquist plot of the EIS spectra. (j) Cycle stability at a current rate of 1C. (k) Long cycle test of the $NiS_2/NiSe_2$@NC/S cell at 3C.

The amount of S and electrolyte are key parameters to evaluate the practical application of LSB. The GCD curves at different current densities of a $NiS_2/NiSe_2$@NC/S-based cell with a relatively high sulfur loading, 6.2 mg cm^{-1}, and a low electrolyte content, 12 μL mg^{-1}, are shown in **Figure 8a**. All the GCD curves exhibit two discharge plateaus and one charge plateau, demonstrating an excellent rate performance (**Figure 8b**) and stability (**Figure 8c**), with a specific capacity of 1058 mAh g^{-1} maintained after 300 cycles at 0.1C. Even when further reducing the electrolyte content to 7.1 μL mg^{-1}, the $NiS_2/NiSe_2$@NC/S cathode was able to maintain a capacity of 720.1mA h g^{-1} after 300 cycles. Finally, pouch cells were assembled using the $NiS_2/NiSe_2$@NC/S cathode (see details in the SI), and their cycling stability was tested. After 150 cycles, the pouch cells retained above 87% of their initial capacity (**Figure 8d**). **Figure 8e** shows how two $NiS_2/NiSe_2$@NC-based pouch cells connected in series can power an LED strip for 15 minutes.

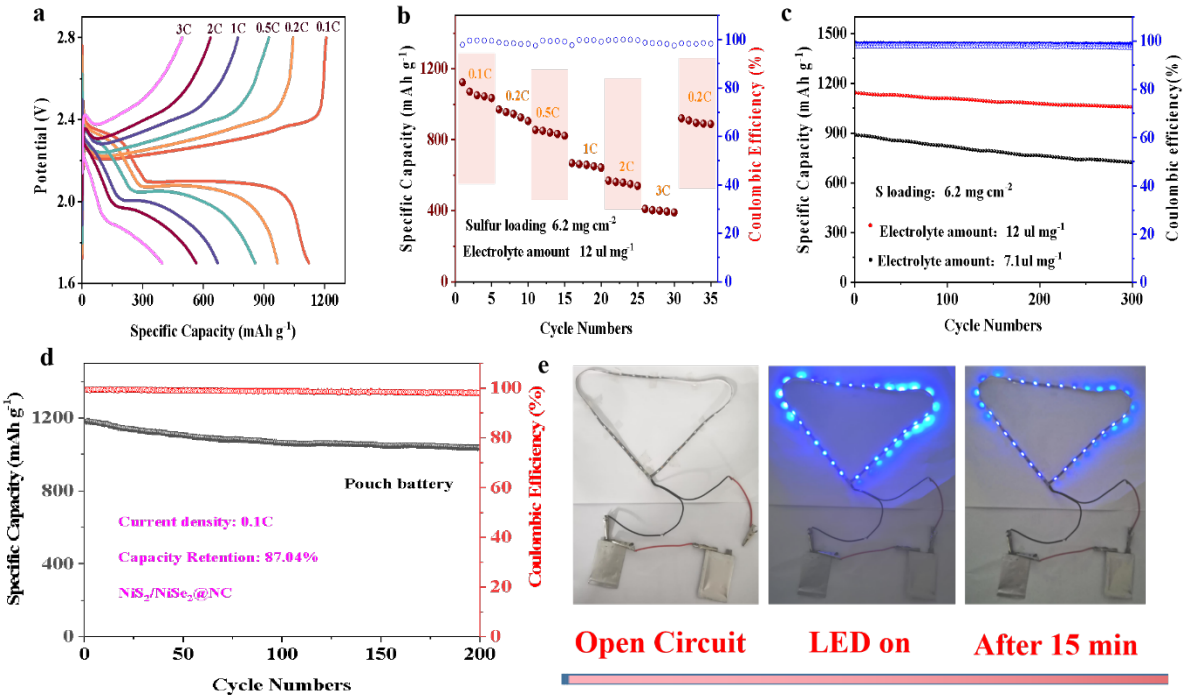

Figure 8. (a) GCD curve of electrode A at high loadings (6.2mg cm^{-2}). (b) Rate performance. (c) Cyclic stability of $NiS_2/NiSe_2$@NC/S at different amounts of electrolyte (0.1C). (d) Long cycle test of pouch cells at 0.1C after 200 cycles. (e) $NiS_2/NiSe_2$@NC/S-based pouch cells connected in series light an LED strip for 15 minutes.

3. Conclusions

In summary, heterostructured $NiS_2/NiSe_2$ particles wrapped within N-doped carbon spheres and displaying a hollow architecture were produced from a Ni-MOF precursor. Magnetic measurements and computational results show the heterostructure to be characterized by Ni^{3+} in a high electronic spin state. $NiS_2/NiSe_2$@C exhibits orbital spin splitting and possesses a high spin configuration with more unpaired electrons. This high spin state regulates the electronic structure resulting in excellent binding strength and catalytic ability toward LiPS. The porous hollow structure not only effectively confines sulfur, but also provides additional buffer space for the electrochemical reaction. $NiS_2/NiSe_2$@NC is used as the host material in the sulfur cathode of LSBs, displaying excellent electrochemical performance. This excellent performance includes a high charge-discharge capacity, excellent rate capability, and long cycle life. This work not only demonstrates the catalytic properties of $NiS_2/NiSe_2$ but also exemplifies the effect of spin polarization in electrocatalytic reactions.

Supporting information

Supporting information is available from the author.

Acknowledgements

This work was financially supported by the SyDECat project from the Spanish MCIN/AEI/FEDER (PID2022-136883OB-C22), the 2BoSS project of the ERA-MIN3 program with the Spanish grant number PCI2022-132985/AEI/10.13039/501100011033, Generalitat de Catalunya 2021 SGR 01581 and 2021 SGR 00457 and European Union NextGenerationEU/PRTR. The authors thank the support from the projects ENE2016-77798-C4-3-R and NANOGEN (PID2020-116093RB-C43), funded by MCIN/ AEI/10.13039/501100011033/ and by "ERDF A way of making Europe", by the "European Union". C.H., J.Y., C.Y.Z., and B.F.N thank the China Scholarship Council for the scholarship support. ICN2 acknowledges the support from the Severo Ochoa Programme (MINECO, grant no. SEV-2017-0706). IREC and ICN2 are both funded by the CERCA Program/Generalitat de Catalunya. This project has received funding from the European Union's Horizon 2020 research and innovation program under grant agreement No 823717-ESTEEM3. These In-situ XRD and XAS experiments were performed at the Melbourne Synchrotron, Australia. J. Li is grateful for the project supported by the Natural Science Foundation of Sichuan (2022NSFSC1229). This study is part of the Advanced Materials programme and was supported by MCIN with funding from European Union NextGenerationEU (PRTR-C17.I1) and by Generalitat de Catalunya. Part of the present work has been performed in the framework of Universitat Autònoma de Barcelona Materials Science PhD program. Authors acknowledge the use of instrumentation as well as the technical advice provided by the Joint Electron Microscopy Center at ALBA (JEMCA). ICN2 acknowledges funding from Grant IU16-014206 (METCAM-FIB) funded by the European Union through the European Regional Development Fund (ERDF), with the support of the Ministry of Research and Universities, Generalitat de Catalunya. ICN2 is founding member of e-DREAM.[X]

Conflict of Interest

The authors declare no conflict of interest.

Data Availability Statement

The data that support the findings of this study are available from the corresponding author upon

reasonable request.

Reference

[1] a) D. Yang, M. Li, X. Zheng, X. Han, C. Zhang, J. Jacas Biendicho, J. Llorca, J. Wang, H. Hao, J. Li, G. Henkelman, J. Arbiol, J. R. Morante, D. Mitlin, S. Chou, A. Cabot, *ACS Nano* **2022**, 16, 11102; b) H. Pan, Z. Cheng, Z. Zhou, S. Xie, W. Zhang, N. Han, W. Guo, J. Fransaer, J. Luo, A. Cabot, M. Wübbenhorst, *Nano-Micro Letters* **2023**, 15, 165.

[2] a) L. Peng, M. Zhang, L. Zheng, Q. Yuan, Z. Yu, J. Shen, Y. Chang, Y. Wang, A. Li, *Small Methods* **2022**, 6, 2200332; b) C. Zhang, R. Du, S. Martí-Sánchez, K. Xiao, D. Yang, C. Zhang, C. Li, G. Zeng, X. Chang, R. He, J. Arbiol, J. Li, J. Jacas Biendicho, A. Cabot, *Energies* **2023**, 16, 4545.

[3] a) X. Lv, T. Lei, B. Wang, W. Chen, Y. Jiao, Y. Hu, Y. Yan, J. Huang, J. Chu, C. Yan, C. Wu, J. Wang, X. Niu, J. Xiong, *Advanced Energy Materials* **2019**, 9, 1901800; b) Y. Gong, Y. Wang, Z. Fang, S. Zhao, Y.-s. He, W. Zhang, J. Mu, L. Zhang, Z.-F. Ma, *Chemical Engineering Journal* **2022**, 446, 136943.

[4] a) C. Zhang, B. Fei, D. Yang, H. Zhan, J. Wang, J. Diao, J. Li, G. Henkelman, D. Cai, J. J. Biendicho, J. R. Morante, A. Cabot, *Advanced Functional Materials* **2022**, 32, 2201322; b) S. Hu, M. Yi, H. Wu, T. Wang, X. Ma, X. Liu, J. Zhang, *Adv. Funct. Mater.* **2022**, 32, 2111084; c) D. Yang, Z. Liang, C. Zhang, J. J. Biendicho, M. Botifoll, M. C. Spadaro, Q. Chen, M. Li, A. Ramon, A. O. Moghaddam, J. Llorca, J. Wang, J. R. Morante, J. Arbiol, S.-L. Chou, A. Cabot, *Advanced Energy Materials* **2021**, 11, 2101250; d) Z. Liang, D. Yang, P. Tang, C. Zhang, J. Jacas Biendicho, Y. Zhang, J. Llorca, X. Wang, J. Li, M. Heggen, J. David, R. E. Dunin-Borkowski, Y. Zhou, J. R. Morante, A. Cabot, J. Arbiol, *Advanced Energy Materials* **2021**, 11, 2170022; e) C. Y. Zhang, L. Gong, C. Zhang, X. Cheng, L. Balcells, G. Zeng, J. J. Biendicho, J. Li, G. Z. Sun, J. Y. Zhou, A. Cabot, *Advanced Functional Materials* **2023**, 33, 2305908; f) C. Y. Zhang, X. Lu, X. Han, J. Yu, C. Zhang, C. Huang, L. Balcells, A. G. Manjón, J. Jacas Biendicho, J. Li, J. Arbiol, G. Sun, J. Y. Zhou, A. Cabot, *Journal of the American Chemical Society* **2023**, 145, 18992.

[5] a) L. Guan, H. Hu, L. Li, Y. Pan, Y. Zhu, Q. Li, H. Guo, K. Wang, Y. Huang, M. Zhang, Y. Yan, Z. Li, X. Teng, J. Yang, J. Xiao, Y. Zhang, X. Wang, M. Wu, *ACS Nano* **2020**, 14, 6222; b) J. Li, C. Chen, Y. Chen, Z. Li, W. Xie, X. Zhang, M. Shao, M. Wei, *Advanced Energy Materials* **2019**, 9, 1901935.

[6] C. Y. Zhang, G. W. Sun, Z. De Shi, Q. Y. Liu, J. L. Pan, Y. C. Wang, H. Zhao, G. Z. Sun, X. P. Gao, X. J. Pan, J. Y. Zhou, *Energy Storage Materials* **2021**, 43, 471.

[7] a) V. P. Ananikov, *ACS Catalysis* **2015**, 5, 1964; b) P. Sabatier, *Catalysis in organic chemistry*, D. Van Nostrand Company, **1922**; c) L. Yang, R. He, X. Wang, T. Yang, T. Zhang, Y. Zuo, X. Lu, Z. Liang, J. Li, J. Arbiol, P. R. Martínez-Alanis, X. Qi, A. Cabot, *Nano Energy* **2023**, 115, 108714.

[8] a) Y. Liu, P. Vijayakumar, Q. Liu, T. Sakthivel, F. Chen, Z. Dai, *Nano-Micro Letters* **2022**, 14, 43; b) J. Li, L. Li, X. Ma, X. Han, C. Xing, X. Qi, R. He, J. Arbiol, H. Pan, J. Zhao, J. Deng, Y. Zhang, Y. Yang, A. Cabot, *Advanced Science* **2023**, 10, 2300841.

[9] J. He, A. Manthiram, *Advanced Energy Materials* **2020**, 10, 2002654.

[10] C. Ye, L. Zhang, C. Guo, D. Li, A. Vasileff, H. Wang, S.-Z. Qiao, *Adv. Funct. Mater.* **2017**, 27, 1702524.

[11] J. Wang, L. Zhou, D. Guo, X. Wang, G. Fang, X. a. Chen, S. Wang, *Small* **2023**, 19, 2206926.

[12] Z. Jin, T. Lin, H. Jia, B. Liu, Q. Zhang, L. Chen, L. Zhang, L. Li, Z. Su, C. Wang, *Nanoscale* **2020**, 12, 16201.

[13] B. Qin, X. Zhao, Q. Wang, W. Yao, Y. Cai, Y. Chen, P. Wang, Y. Zou, J. Cao, X. Zheng, J. Qi, W. Cai, *Energy Storage Materials* **2023**, 55, 445.

[14] T. L. L. Doan, D. C. Nguyen, R. Amaral, N. Y. Dzade, C. S. Kim, C. H. Park, *Applied Catalysis B: Environmental* **2022**, 319, 121934.

[15] X. Han, L. Zhao, Y. Liang, J. Wang, Y. Long, Z. Zhou, Y. Zhang, Y. Li, J. Ma, *Advanced Energy Materials* **2022**, 12, 2202747.

[16] a) Z.-y. Mei, G. Zhao, C. Xia, S. Cai, Q. Jing, X. Sheng, H. Wang, X. Zou, L. Wang, H. Guo, B. Y. Xia, *Angewandte Chemie International Edition* **2023**, 62, e202303871; b) Y. Li, Y. Ji, Y. Zhao, J. Chen, S. Zheng, X. Sang, B. Yang, Z. Li, L. Lei, Z. Wen, X. Feng, Y. Hou, *Advanced Materials* **2022**, 34, 2202240; c) Q. Wang, T. Liu, K. Chen, D. Wu, C. Chen, M. Chen, X. Ma, J. Xu, T. Yao, Y. Li, H. Zhou, Y. Wu, *Small* **2022**, 18, 2204015; d) Y. Wang, P. Meng, Z. Yang, M. Jiang, J. Yang, H. Li, J. Zhang, B. Sun, C. Fu, *Angewandte Chemie International Edition* **2023**, 62, e202304229; e) D. Wu, H.-Q. Yin, Z. Wang, M. Zhou, C. Yu, J. Wu, H. Miao, T. Yamamoto, W. Zhaxi, Z. Huang, L. Liu, W. Huang, W. Zhong, Y. Einaga, J. Jiang, Z.-M. Zhang, *Angewandte Chemie International Edition* **2023**, 62, e202301925; f) T. He, Y. Chen, Q. Liu, B. Lu, X. Song, H. Liu, M. Liu, Y.-N. Liu, Y. Zhang, X. Ouyang, S. Chen, *Angewandte Chemie International Edition* **2022**, 61, e202201007; g) Z. Zhao, M. Hu, T. Nie, W. Zhou, B. Pan, B. Xing, L. Zhu, *Environmental Science & Technology* **2023**, 57, 4556.

[17] a) Q. Zhang, R. Ao, R. Gao, H. Yang, *Inorganic Chemistry* **2022**, 61, 19780; b) C. Y. Zhang, C. Zhang, G. W. Sun, J. L. Pan, L. Gong, G. Z. Sun, J. J. Biendicho, L. Balcells, X. L. Fan, J. R. Morante, J. Y. Zhou, A. Cabot, *Angewandte*

Chemie International Edition **2022**, 61, e202211570.

[18] H. Li, M. Chuai, X. Xiao, Y. Jia, B. Chen, C. Li, Z. Piao, Z. Lao, M. Zhang, R. Gao, B. Zhang, Z. Han, J. Yang, G. Zhou, *Journal of the American Chemical Society* **2023**, 145, 22516.

[19] M. Li, Y. Liu, Y. Zhang, X. Han, T. Zhang, Y. Zuo, C. Xie, K. Xiao, J. Arbiol, J. Llorca, M. Ibáñez, J. Liu, A. Cabot, *ACS Nano* **2021**, 15, 4967.

[20] a) S. Ni, H. Qu, Z. Xu, X. Zhu, L. Chen, H. Xing, X. Wu, H. Liu, L. Yang, *ACS Applied Materials & Interfaces* **2023**, 15, 36423; b) R. Liang, C. Shu, A. Hu, M. Li, Z. Ran, R. Zheng, J. Long, *Chemical Engineering Journal* **2020**, 393, 124592.

[21] J. Zhu, W. Tu, H. Pan, H. Zhang, B. Liu, Y. Cheng, Z. Deng, H. Zhang, *ACS Nano* **2020**, 14, 5780.

[22] a) C. Huang, S. Lv, A. Gao, J. Ling, F. Yi, J. Hao, M. Wang, Z. Luo, D. Shu, *Chemical Engineering Journal* **2022**, 431, 134083; b) C. Huang, A. Gao, F. Yi, Y. Wang, D. Shu, Y. Liang, Z. Zhu, J. Ling, J. Hao, *Chemical Engineering Journal* **2021**, 419, 129643.

[23] a) A. Muthurasu, P. Sampath, T. H. Ko, P. C. Lohani, I. Pathak, D. Acharya, K. Chhetri, D. H. Kim, H. Y. Kim, *Applied Catalysis B: Environmental* **2023**, 330, 122523; b) Y. Wang, Y. Wang, H. Gao, Z. Huang, Q. Hao, B. Liu, *Chemical Engineering Journal* **2023**, 451, 138515.

[24] J. Luo, Y. Liu, H. Xiao, Y. Wang, Y. Mao, Y. Zhang, Y. Su, Y. Xia, S. Chen, Q. Deng, Z. Zeng, S. Deng, J. Wang, *Chemical Engineering Journal* **2023**, 451, 138677.

[25] F. Zhou, R. Wang, S. He, X. Liu, S. Liu, H. Shao, X. Liu, Z. Xiao, J. Liu, *Adv. Funct. Mater.* **2023**, 33, 2211124.

[26] F. Zou, Y.-M. Chen, K. Liu, Z. Yu, W. Liang, S. M. Bhaway, M. Gao, Y. Zhu, *ACS Nano* **2016**, 10, 377.

[27] X. Liu, F. Zou, K. Liu, Z. Qiang, C. J. Taubert, P. Ustriyana, B. D. Vogt, Y. Zhu, *Journal of Materials Chemistry A* **2017**, 5, 11781.

[28] a) S. Jiang, F. Chen, L. Zhu, Z. Yang, Y. Lin, Q. Xu, Y. Wang, *ACS Applied Materials & Interfaces* **2022**, 14, 10227; b) N. S. McIntyre, M. G. Cook, *Analytical Chemistry* **1975**, 47, 2208.

[29] Z. Xue, X. Li, Q. Liu, M. Cai, K. Liu, M. Liu, Z. Ke, X. Liu, G. Li, *Advanced Materials* **2019**, 31, 1900430.

[30] a) Q. Li, R. Deng, Y. Chen, J. Gong, P. Wang, Q. Zheng, Y. Huo, F. Xie, X. Wei, C. Yang, *Small* **2023**, 2303642; b) H. Deng, L. Yao, Q.-A. Huang, Q. Su, J. Zhang, F. Zhang, G. Du, *RSC advances* **2017**, 7, 9819; c) Z. Li, X. Yu, A. Gu, H. Tang, L. Wang, Z. Lou, *Nanotechnology* **2017**, 28, 065406; d) S. R. S, D. Punnoose, J.-H. Bae, I. K. Durga, C. V. Thulasi-Varma, B. Naresh, A. Subramanian, V. Raman, H.-J. Kim, *Electrochimica Acta* **2017**, 254, 269; e) J.-Y. Luo,

F.-C. Hu, B.-J. Xi, Q.-W. Han, X.-Q. Wu, Y.-P. Wu, Q. Zhang, R. Chi, D.-S. Li, *Inorganic Chemistry Communications* **2022**, 143, 109777; f) J. Li, Z. Ding, J. Li, C. Wang, L. Pan, G. Wang, *Chemical Engineering Journal* **2021**, 407, 127199; g) C. Zhou, S. Wan, Y. Chen, L. Fu, H. Chen, C. Kang, Q. Liu, *Journal of Power Sources* **2021**, 509, 230401.

[31] W. Bao, L. Liu, C. Wang, S. Choi, D. Wang, G. Wang, *Advanced Energy Materials* **2018**, 8, 1870060.

[32] C. Huang, J. Yu, C. Li, Z. Cui, C. Zhang, C. Zhang, B. Nan, J. Li, J. Arbiol, A. Cabot, *Adv. Funct. Mater.* **2023**, n/a, 2305624.

[33] C. Zhang, R. Du, J. J. Biendicho, M. Yi, K. Xiao, D. Yang, T. Zhang, X. Wang, J. Arbiol, J. Llorca, Y. Zhou, J. R. Morante, A. Cabot, *Advanced Energy Materials* **2021**, 11, 2100432.

[34] a) D. Fang, G. Wang, S. Huang, T. Chen Li, J. Yu, D. Xiong, D. Yan, X. Liang Li, J. Zhang, Y. Von Lim, S. A. Yang, H. Ying Yang, *Chemical Engineering Journal* **2021**, 411, 128546; b) Q. Hao, G. Cui, Y. Zhang, J. Li, Z. Zhang, *Chemical Engineering Journal* **2020**, 381, 122672; c) D. Lu, X. Wang, Y. Hu, L. Yue, Z. Shao, W. Zhou, L. Chen, W. Wang, Y. Li, *Adv. Funct. Mater.* **2023**, 33, 2212689; d) L. Wu, J. Hu, X. Yang, Z. Liang, S. Chen, L. Liu, H. Hou, J. Yang, *Journal of Materials Chemistry A* **2022**, 10, 23811; e) Z. Wu, S. Chen, L. Wang, Q. Deng, Z. Zeng, J. Wang, S. Deng, *Energy Storage Materials* **2021**, 38, 381; f) S. Chen, J. Luo, N. Li, X. Han, J. Wang, Q. Deng, Z. Zeng, S. Deng, *Energy Storage Materials* **2020**, 30, 187.

[35] H. Zhang, S. Xin, J. Li, H. Cui, Y. Liu, Y. Yang, M. Wang, *Nano Energy* **2021**, 85, 106011.

[36] W. Liu, C. Luo, S. Zhang, B. Zhang, J. Ma, X. Wang, W. Liu, Z. Li, Q.-H. Yang, W. Lv, *ACS Nano* **2021**, 15, 7491.

[37] C. Zhang, J. J. Biendicho, T. Zhang, R. Du, J. Li, X. Yang, J. Arbiol, Y. Zhou, J. R. Morante, A. Cabot, *Adv. Funct. Mater.* **2019**, 29, 1903842.

[38] R. Chu, T. T. Nguyen, Y. Bai, N. H. Kim, J. H. Lee, *Advanced Energy Materials* **2022**, 12, 2102805.